Research article

Complex rhythm and synchronization of half-center oscillators under electromagnetic induction

Feibiao Zhan[1] **and Jian Song**[2,3,*]

[1] School of Mathematics, Nanjing Audit University, Nanjing 211815, China

[2] School of Mathematics, South China University of Technology, Guangzhou 510640, China

[3] School of Mathematical and Computational Sciences, Massey University, Auckland 4442, New Zealand

* **Correspondence:** Email: masongj_vlp@mail.scut.edu.cn.

Abstract: Half-center oscillators are typical small circuits that are crucial for understanding CPG. The complex rhythms of CPG are closely related to certain diseases, such as epilepsy. This paper considered the influence of electromagnetic induction on the discharge mode of the half-center oscillators. First, we analyzed the response of individual firing neuron rhythms to electromagnetic induction when the slow-variable parameters vary. We also discussed the changes in the dynamic bifurcation structure when the intensity of electromagnetic induction varies. Furthermore, we determined the effects of mutually inhibitory and self-inhibitory synaptic parameters on the firing rhythm of the half-center oscillators. The different responses induced by electromagnetic induction interventions, showed that mutually inhibitory synapses modulate the firing rhythm weakly and self-inhibition synapses have a significant impact on firing rhythm. Finally, with the change of synaptic parameter values, the combined effects of autapse and mutually inhibitory synapses on the discharge rhythm of half-center oscillators were analyzed in symmetric and asymmetric autapse modes. It was found that the synchronous state of the half-center oscillators had a more robust electromagnetic induction response than the asynchronous state.

Keywords: complex rhythm; half-center oscillators; synchronization; neuron model; electromagnetic induction

1. Introduction

Central pattern generator (CPG) rhythms have been discovered in invertebrates such as crustacean pyloric or gastric and leech heartbeats. CPGs are typical small circuits of neural networks, providing a new perspective on how circuit dynamics depend on neurons and synapses. CPG can spontaneously

generate multiple rhythmic patterns in the absence of external stimuli [1, 2], and it is associated with various motor behaviors, such as swimming and walking [3, 4]. The characteristics of CPG are described as the stability and robustness of the firing rhythm of neuronal small circuits. Recently, a large amount of research has focused on the working mechanism of CPG from both theoretical and experimental perspectives, providing a biological theoretical basis for the study of CPG-inspired rhythmic motion control [5–8]. Still, only some have directly studied the discharge rhythm of CPG. However, how to efficiently control and use the flexibility and robustness of CPG to guide research inspired by it is still being explored. Some researchers believe that the connection of CPG forms attractors, and each attractor corresponds to a rhythmic motor behavior [9]. Theoretical researchers have explained the potential internal mechanisms of CPG from a dynamic perspective [10], revealing the mechanism of the emergence, disappearance, and stabilization of neuronal rhythms in a tri-neuron network with mutual inhibition under changes in synaptic parameters. Lu et al. investigated the synchronization and stochastic resonance characteristics of small-world networks based on CPG [11]. Researchers have studied the impact of transient input on neuronal firing using phase response curves [12, 13].

Recent studies have shown how the morphology of neurons can significantly affect the rhythmic patterns of CPG circuits [14]. There are many studies on the mechanism of neuronal rhythm generation [15–19], but it is unclear whether the different firing mechanisms of neurons mean the diversity of CPG circuit functions. Can the same CPG circuit generate multiple motion behaviors, making its motion functions diverse [20, 21]. Research has shown that the generation of motor behavior depends on the rhythmic modulation of CPG. One proposal suggests that the CPG rhythm pattern can simulate the human central system's rhythmic activity and control the arm movement rhythm [22]. In addition, CPG rhythm patterns can improve the diagnosis of multiple diseases. For instance, Mader et al. [1] explained that CPG can assist in developing therapeutic methods for the recovery of spinal solid cord injuries. Tassinari et al. reviewed the relationship of central pattern generators with parasomnias and sleep-related epileptic seizures. They explained some epileptic seizures and parasomnias using the rhythm patterns of the CPG [23, 24]. Therefore, studying the functioning principle of CPG rhythm activities is essential for understanding related motor behaviors, improving motor control and disease diagnosis. It is necessary to examine the diversity of rhythm patterns to understand the function of CPG. The study of CPG rhythm patterns has recently been discussed [25, 26].

A half-center oscillator (HCO) is a unit composed of two neurons that mutually inhibit each other, and studying the rhythmic pattern of HCO is crucial for understanding CPG [27, 28]. Studying motion control is facilitated by the easy identification of HCO rhythm patterns. Researchers discussed how neuron parameters affect the rhythmic patterns of HCO to achieve motion control [29], and analyze how the system parameter space changes the robustness of HCO rhythmic patterns [30]. Recently, delayed half-center oscillator (DHCO) in-phase and antiphase dynamics behavior and the coexistence of multiple routes leads to chaos was studied [31, 32]. Noise closely affects the robustness of HCO rhythm patterns [33], and the impact of electromagnetic induction on neuronal firing rhythms and diseases such as epilepsy cannot be ignored [34, 35]. Few people have paid attention to the effects of electromagnetic induction and connection modes on the HCO discharge rhythm. Here, the synaptic conductance parameters and the effects of electromagnetic induction on the HCO rhythm pattern are analyzed. Mutual inhibitory neurons can improve the stability of HCO. Here, we explore the rhythmic pattern of HCO under electromagnetic induction, and a model containing self-inhibitory synapses and mutual inhibitory synapses is established. We examine the impact of electromagnetic induction and

connection modes on the HCO rhythm pattern.

This study investigates complex rhythm and synchronization of HCOs under electromagnetic induction. First, the dynamic changes of individual neurons under electromagnetic induction are analyzed. Moreover, we discuss the effects of mutual inhibition and self-inhibition synaptic parameters on the rhythmic patterns of HCO and show their different responses to electromagnetic induction. The results indicate that mutual inhibition has a weaker effect on the discharge rhythm than self-inhibition. The study examines the impact of self-inhibition synapses, mutual inhibitory synapses, and electromagnetic induction on the HCO rhythm pattern, both symmetrically and asymmetrically. It has been found that the synchronous state of the HCO exhibits a more robust electromagnetic induction response than the asynchronous state. Rhythm patterns are closely related to motor control. The research of rhythmic patterns of small circuits contributes to the development of intelligent science. Intelligent science is inspired by the principle of biological CPG and the establishment of spiking neural networks [36, 37].

The paper is organized as follows. Section 2 presents the materials and methods we used to build HCO, including the Hodgkin–Huxley (HH) neuron model. Then, Section 3.1 illustrates the rhythmic discharge of HCOs with different synaptic coupling. Section 3.2 investigates the synchronization of HCOs with different symmetric and asymmetric autapses. Finally, we have a discussion and conclusion in Section 4.

2. Materials and methods

2.1. Neuronal model and dynamics under electromagnetic induction

In our CPG, each interneuron is modeled by a simplified HH model. Variable ϕ denotes the magnetic flux across the membrane, and $\rho(\phi)$ represents the incremental memductance function of flux controlled memristor [38], which is used to describe the coupling between membrane potential and magnetic flux. The incremental memductance function is often described by $\rho(\phi) = \alpha + 3\beta\phi^2$, and α, β are fixed parameters [38, 39]. The term $k\rho(\phi)V$ could be viewed as induction current on the membrane as follows:

$$i' = \frac{dq(\phi)}{dt} = \frac{dq(\phi)}{d\phi}\frac{d\phi}{dt} = \rho(\phi)V_0 = k\rho(\phi)V.$$

This microcircuit captures the dynamics by a single compartment, which is described by the following differential equations [17, 34, 40]:

$$\begin{aligned}
C_m\frac{dV}{dt} &= -I_{Na} - I_K - I_{Leak} + I + k\rho(\phi)V, \\
\frac{dn}{dt} &= \frac{n_\infty - n}{\tau_n}, \\
\frac{dI}{dt} &= \varepsilon(-80 - V). \\
\frac{d\phi}{dt} &= (k_1 V - k_2\phi).
\end{aligned} \tag{2.1}$$

Here, C_m denotes the neural membrane capacitance density ($\mu F/cm^2$); V represents the membrane potential (mV); the gating variable n of activated K^+ channels denotes the activation probability of

potassium ion channels; the h variable (the formulations of I_{Na} in the original model) represents a merged refractory variable (Na^+ inactivation and K^+ activation). It is replaced by $1-n$ in the simplified HH model. So, the n gate appears in the formulations of I_{Na}. τ_n is the time constant (ms); I is a voltage-dependent linear control current; electromagnetic induction parameters are $\alpha = 0.1, \beta = 0.02, k_1 = 0.9, k_2 = 0.5$; and I_{Na}, I_K, and I_{Leak} are sodium ion current, potassium ion current, and leakage current. Their expressions are as follows.

$$
\begin{aligned}
I_{Na} &= g_{Na} m_\infty(V) (1-n) (V - E_{Na}), \\
I_K &= g_K n (V - E_K), \\
I_{Leak} &= g_L (V - E_L),
\end{aligned}
$$

where the parameters g_{Na} and g_K are the maximal conductances (mS/cm^2); E_{Na}, E_K, and E_L are the reversal potentials (mV); and m_∞ and n_∞ are the steady-state of the ionic gating channels. They are modeled using:

$$
m_\infty(V) = \frac{1}{1 + exp\left(-\dfrac{V + 35}{5}\right)}, n_\infty(V) = \frac{1}{1 + exp\left(-\dfrac{V + 36}{5}\right)}.
$$
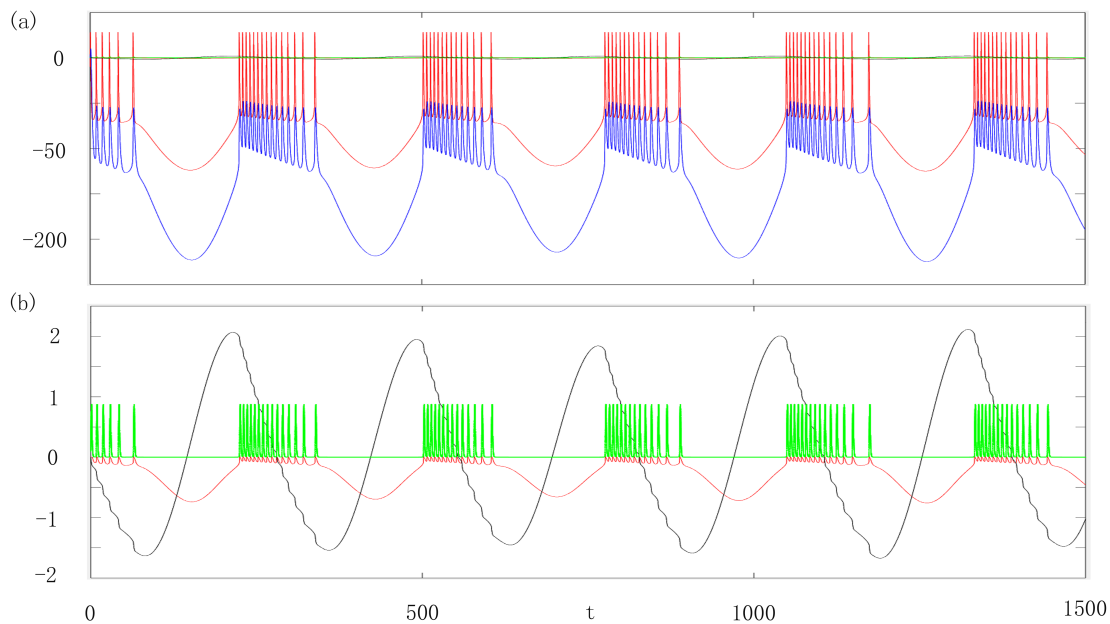
Figure 1. Time series diagrams of various variables in the neuron model under electromagnetic induction. (a) The red trajectory represents the potential time series, the blue trajectory represents the electromagnetic induction sequence diagram, and three-time series diagrams are next to the green trajectory near the zero line. (b) The enlarged image near the zero line in the Figure (a), where red represents $\rho(\phi)$, green represents the gating variable n, and black represents the feedback current I. Electromagnetic induction parameters $k = 0.00002$, $\varepsilon = 0.001$.

First, we present a time series diagram of the neuron model under electromagnetic induction. It is

found that the membrane potential of neurons exhibits a regular burster discharge pattern (in the Figure 1 red trace), and the time series of the electromagnetic induction parameter ϕ (in the Figure 1 blue trace) and the peak time of the membrane potential sequence are synchronous. The electromagnetic induction parameter ϕ affects the membrane potential of neurons at all times, although their amplitudes differ. The neuronal membrane potential strongly responds to the fluctuations of electromagnetic induction parameter ϕ. We enlarge the green curve near the zero line in the Figure 1(a) to obtain Figure 1(b), where the green trajectory represents the time series of the gating variable; the black trajectory represents the feedback current I, which is a slow regulating variable. The red trajectory shows the sequence diagram of the electromagnetic induction term $\rho(\phi)$ changing over time. Figure 1(b) shows that compared to the slowly regulated variable I, the change in the electromagnetic induction term is weaker, but the regulation of the system variables does not weaken. Its impact on the system is equivalent to adding external stimuli that change over time with a red trajectory and the membrane potential time series displayed by the system under this external stimulus. Below, we will provide the trend of the dynamic bifurcation diagram of the system as the electromagnetic induction parameters change.
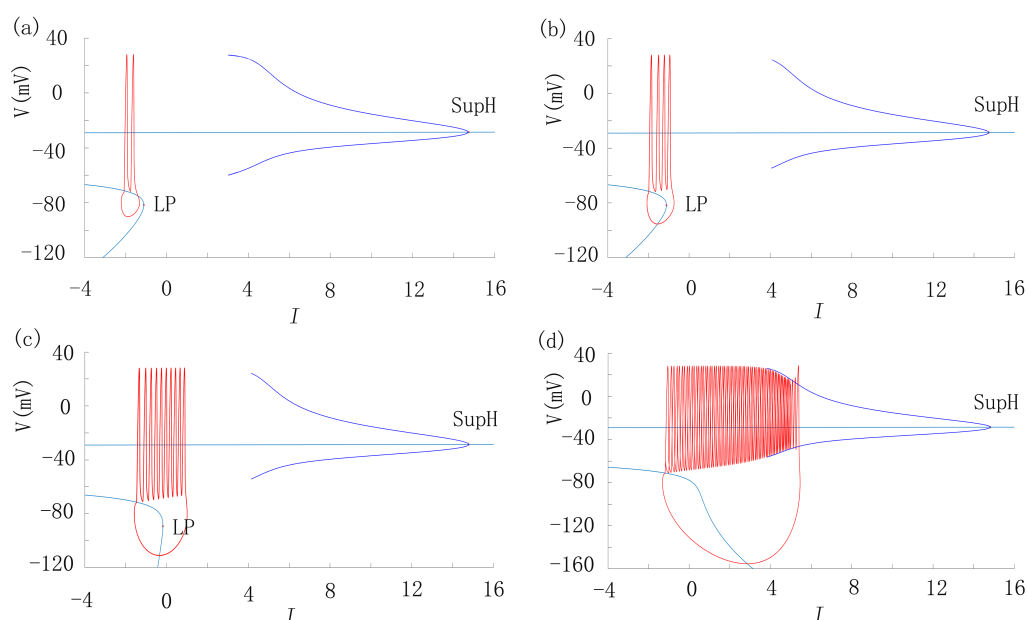
Figure 2. The bifurcation diagram of fast-slow dynamics varies with the electromagnetic induction parameters. Red represents the phase trajectory; blue represents the maximum and minimum values of the limit cycle; and green represents the equilibrium point curve. Here *LP* represents the saddle-node, and *supH* represents the supercritical Hopf point. Parameter $\varepsilon = 0.001$; the electromagnetic induction parameters k are -0.000012, -0.000008, 0, 0.000005 (from (a) to (d)), respectively.

From the above analysis, we know that the neuronal system's membrane potential strongly responds to electromagnetic induction as an external stimulus. Here, we take the feedback current I of the system as a slow variable and provide a bifurcation diagram of the system with the participation of electromagnetic induction. First, we can see that the system membrane potential exhibits burster discharge with ten peaks per burster when the electromagnetic induction parameter $k = 0$ (in the Figure 2(c)).

With k increased to 0.000005, the positive response of the system membrane potential to electromagnetic induction leads to a significant increase in the number of peaks per burster (in the Figure 2(d)). Based on the review about classication of bursters [15], here may show a Circle/Circle bifurcation type. With k reduced to -0.000008, electromagnetic induction exhibits inhibition of action potential, resulting in burster discharge of membrane potential with only 4 peaks appearing in each burster (in the Figure 2(b)). When the electromagnetic induction $k = -0.000012$, the membrane potential exhibits 2 peaks per burster (in the Figure 2(a)). If the electromagnetic induction k further decreases, the system membrane potential sequence will exhibit a single spiking.
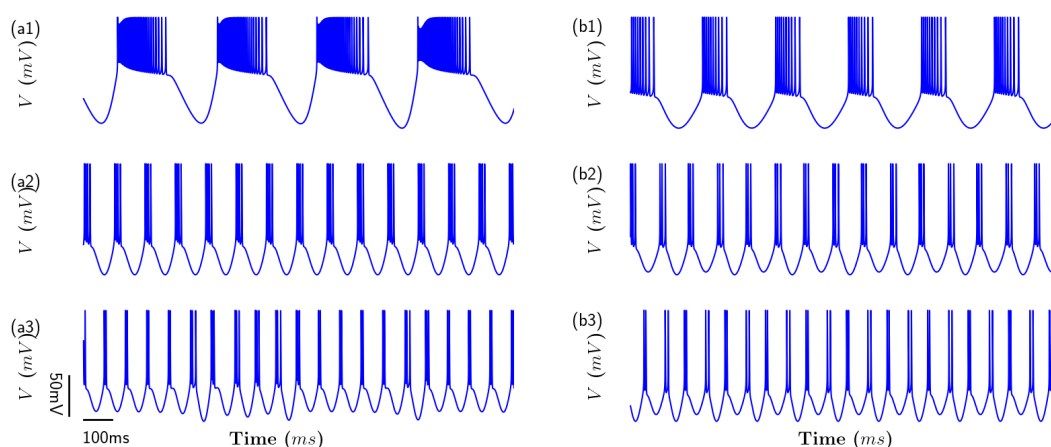
Figure 3. Time series diagram of membrane potential. The parameters ε from top to bottom are equal to 0.001, 0.005, and 0.01, respectively. On the left side is electromagnetic induction intervention, parameter $k = 0.00005$; there is no electromagnetic induction on the right side.

Here, we investigate the dynamic changes in membrane potential discharge rhythm by adding electromagnetic induction under different slow variable parameters ε. In the Figure 3, we can see that the discharge rhythm of the membrane potential exhibits a regular rectangular wave burster (in the Figure 3(b1)) when the parameter $\varepsilon = 0.001$, and the discharge rhythm of the membrane potential exhibits a parabolic burster when electromagnetic induction is added to the system (in the Figure 3(a1)). The number of peaks per burster significantly increases. When the parameter $\varepsilon = 0.005$, the system exhibits a regular burster discharge rhythm pattern, and the number of bursters within the same time interval significantly increases (in the Figure 3(b2)), and the burster interval decreases. The addition of electromagnetic induction transforms the discharge rhythm of the membrane potential from an initial irregular burster to a regular burster, and the number of peaks per burster increases (in the Figure 3(a2)). The membrane potential of the system exhibits a periodic burster when the parameter $\varepsilon = 0.01$ (in the Figure 3(b3)), and two peaks appear in each burster, with a smaller burster interval than the first two groups. Adding electromagnetic induction results in an irregular discharge rhythm of the membrane potential. The system's sensitivity increases with the addition of electromagnetic induction under this parameter (in the Figure 3(a3)). In summary, electromagnetic induction significantly impacts the membrane potential rhythm of individual neurons.

2.2. HCOs-based model
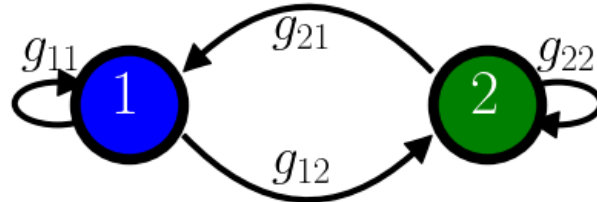
Figure 4. Connection diagram of an improved HCO with autapse (coupled system with chemical synapse). The solid blue and green circles represent neurons and are labeled as 1 and 2, respectively. These neurons are modeled by the HH model; see Eq (2.1). Black filled arrows represent inhibitory synapses; see Eq (2.2). The conductance of the connection between neurons is noted as g_{ij}, $i, j = 1, 2$. This indicates that the synapse is from neuron i to neuron j.

Next, we will consider the improved firing rhythm of two neurons that mutually inhibit each other, also known as HCOs. We have added two self-synapses of neurons here. Considering how the synchronization of neurons changes with changes in two sets of synaptic parameters, we first examine whether inhibition from autapse and mutual inhibition is consistent. Furthermore, we research HCOs in both symmetric and asymmetric autapse modes. When only g_{12} is not 0 and only g_{11} or g_{22} is not 0, we investigate the difference in the firing rhythm of neurons. The inhibitory relationship between neurons is a crucial factor in rhythm generation. The most common structure describing firing rhythmic activities consists of two coupled neurons that inhibit each other (in the Figure 4). This structure is widely known as an HCO and is symmetrically coupled through both inhibitory connections with g_{12} and g_{21}. We will start with the most straightforward network where two cells next section and extended self-inhibition from neurons. Neurons are color-coded (blue and green) based on firing activity. The synaptic transmission in the structure of the HCO in the Figure 4 is ionotropic synapses. First-order kinetic equations model these synapses, which are inhibitory and conductance-based, similar to previous studies [41–44]:

$$\begin{cases} I_{pre \to post} & = g_{pre \to post} H_\infty(V_{pre})\left(V_{pre} - E_{pre \to post}\right), \\ H_\infty(V_{pre}) & = \dfrac{1}{1 + exp\left(-\dfrac{V_{pre} - \theta}{\sigma}\right)}. \end{cases} \tag{2.2}$$

Here, V_{pre} is the presynaptic voltage, $\sigma = 1mV$ is the steepness, $\theta = -60mV$ sets the value when the function is semi-activated, $E_{pre \to post} = -110$ is the reversal potential, and $g_{pre \to post}$ is the maximal conductance (g_{ij}, $i, j = 1, 2$ in the Figure 4).

For numerical integration of network system, the fourth-order Runge–Kutta algorithm was used with a time step of 0.05 ms. The total integration time length of each simulation run was 5000 ms.

Simulations were implemented in Python 3.9.7 on PC with $12th$ Gen Intel(R) Core(TM) i7-12700H 2.30 GHz CPU.

3. Results

### 3.1. Rhythmic discharge of HCOs with different synaptic coupling
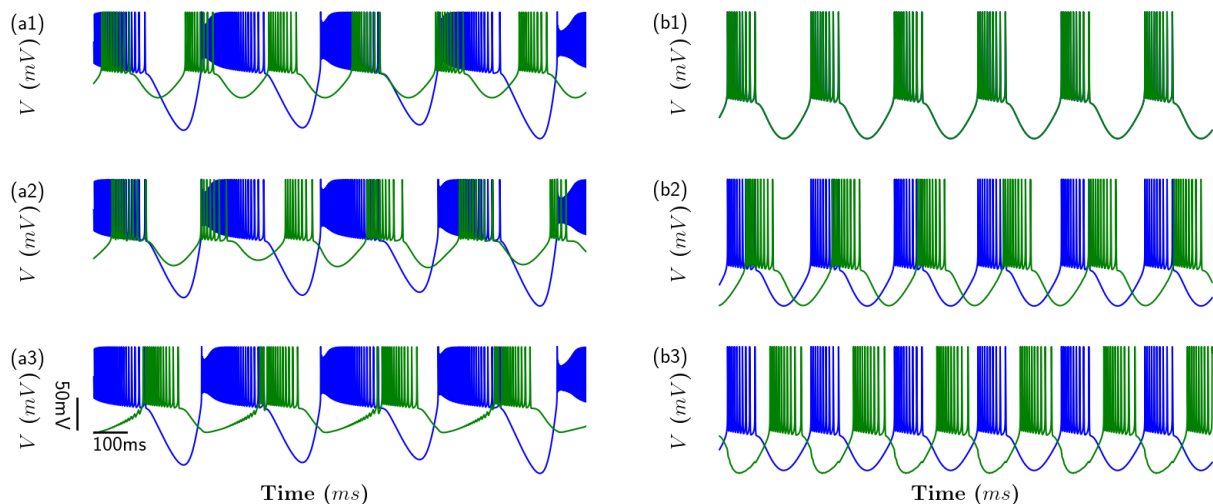
Figure 5. The discharge rhythm of HCOs when there is only one synaptic conductance change, i.e., when g_{12} changes. Here, $g_{11} = g_{21} = g_{22} = 0$. The coupling conductance parameters g_{12} from top to bottom are 0, 0.02, and 0.2, respectively. On the right side is no added electromagnetic induction; on the left, there is added electromagnetic induction, and the parameter $k = 0.00005$ only stimulates neuron 1. Blue represents the membrane potential sequence of neuron 1, and green represents the membrane potential sequence of neuron 2.

The section discusses the reciprocal inhibition between two neurons, which are HCOs (in the Figure 4). The synchronous firing of neurons contains essential neural information. Here, we investigate the synchrony of HCO rhythm activity. First, we investigate the firing rhythm when the synaptic conductance g_{12} is not zero; only neuron 1 inhibits neuron 2. When $g_{12} = 0$, neurons 1 and 2 have a wholly synchronized discharge pattern (in the Figure 5(b1)), which is reasonable. By changing g_{12} to 0.02 in Figure 5(b2), it is found that the firing rhythm of neuron 1 does not change, while the firing rhythm of neuron 2 gradually changed from the state of synchronous neuron 1 (the first two burster patterns) to an asynchronous state, until it reached an asynchronous state. When $g_{12} = 0.2$, the discharge mode of neuron 1 remains unchanged, and the discharge modes of the two neurons directly exhibit a strictly asynchronous state (in the Figure 5(b3)), with the burster mode states of neurons 1 and 2 alternating. We obtain the firing rhythm on the left side of Figure 5 when only neuron 1 in the system adds electromagnetic induction. We can observe that the rhythmic pattern of neuron 1 under electromagnetic induction is consistent under all three sets of coupled conductance parameters. Under weak coupling conductance ($g_{12} = 0.02$), the rhythmic pattern of neuron 2 transitions to irregular discharge, meaning that the discharge rhythm of neuron 2 is greatly affected by electromagnetic induction (in the Figure 5(a2)). At a relatively strong coupling conductance coefficient ($g_{12} = 0.2$) (in the Figure 5(a3)),

the burster firing rhythm pattern of neuron 2 is strengthened. We can see a significant increase in the number of peaks per burster, and the stability of the burster pattern is also more robust.
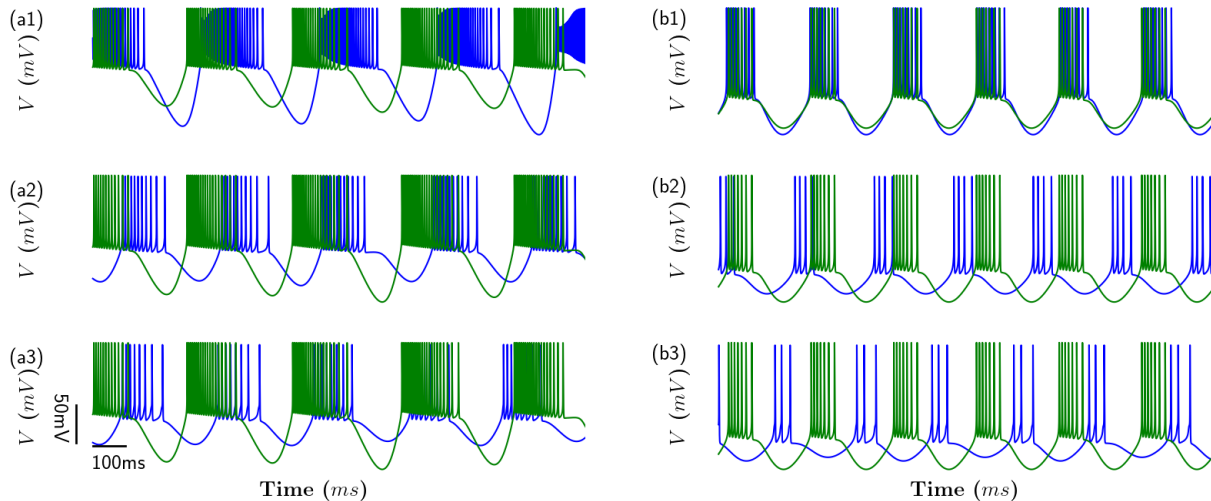
Figure 6. The discharge rhythm of HCOs. Only when the self-inhibitory synaptic conductance is not 0, that is, when only g_{11} is changed, here $g_{12} = g_{21} = 0$. As a comparison, we always take $g_{22} = 0.05$ in all the figures. The coupling conductance parameters g_{11} from top to bottom are 0, 0.2, and 0.35, respectively. On the right side, there is no added electromagnetic induction; on the left, there is added electromagnetic induction, and the parameter $k = 0.00005$. Neurons 1 and 2 are both being stimulated at the same time. Blue represents the membrane potential sequence of neuron 1, and green represents the membrane potential sequence of neuron 2.

Here, we consider the discharge rhythm when the self-inhibitory synaptic conductance changes, where $g_{12} = g_{21} = 0$. It is evident from the righthand side of Figure 6 that the firing neuron 2 has a consistent firing rhythm, unaffected by neuron 1 within a fixed g_{22}. Its firing rhythm is different from that when the coupling conductance $g_{11} = 0$ (blue trace in the Figure 6(b1)), and at this point, the firing rhythm of neuron 1 (in the Figure 6(b1)) is entirely consistent with that of neuron 1 in the Figure 5(b1). In the Figure 6(b2), when $g_{11} = 0.2$, neuron 1 shows a regular burster pattern with four peaks in each burster. This pattern is distinct from the firing rhythm pattern in the Figure 5(b3), where the coupling parameter g_{12} between neuron 1 and neuron 2 is 0.2. The different firing patterns might indicate that the inhibitory effects of autapse and mutually inhibitory synaptic conductance on neurons are different. This is an exciting observation worth noting. Here, self-inhibition reduces the number of peaks per burster in neuron 1 (in the Figure 6(b2)). When increasing g_{11} to 0.35, the discharge pattern of neuron 1 exhibits an irregular rhythm, appearing to be a burster pattern with three peaks in each burster (in the Figure 6(b3)). Continuing to increase the self-coupling synaptic conductance g_{11}, the firing rhythm of neuron 1 may transform into a burster rhythm pattern with two peaks in each burster and a regular burster discharge pattern, which is not shown here. These all indicate that self-synaptic coupling is essential to regulating the diversity of discharge rhythms. The left side of Figure 6 shows the discharge

rhythm pattern obtained by adding electromagnetic induction to the system. In all three cases, the discharge pattern of neuron 2 is undoubtedly wholly consistent. The firing pattern of neuron 1 (in the Figure 6(b1)) is consistent with the firing rhythm of neuron 1 in the Figure 5(b1) when $g_{11} = 0.2$ (in the Figure 6(a2)), and the addition of electromagnetic induction increases the number of peaks per burster in the neuron 1. When $g_{11} = 0.35$, the irregular discharge pattern of neuron 1 remains irregular under electromagnetic induction as if the number of peaks in each burster increases. Under these three types of autapse, perhaps electromagnetic induction enhances the discharge of membrane potential. We also found that the impact of electromagnetic induction on the discharge mode of HCOs varies depending on the different synaptic connections. The effects of self-synaptic inhibition and mutual inhibition on the firing patterns of neurons are also other, as shown by comparing Figures 5 and 6. Therefore, this suggests that the effects of electromagnetic induction on HCOs must be carefully considered in terms of their synaptic connections.

### 3.2. Synchronization of HCOs with different symmetric and asymmetric autapse

Here, we examine the synchronization state of two neurons with a half-center oscillator by phase difference $\Delta^{(n)}$ and average phase difference $S = \frac{1}{N} \sum_{n=1}^{N} \Delta^{(n)}$ (N is the number of samples within the range of values of the vertical coordinate parameter) [45], as shown in the Figure 7. Figure 7(a1) shows the branch diagram of the phase difference when two mutually inhibitory coupling conductance and self-synaptic conductance are equal, respectively, under the introduction of electromagnetic induction in neuron 1. The calculation results show that, without introducing electromagnetic induction, the HCO exhibits a fully synchronized state. We will discuss the discharge mode of the HCO under symmetric self-synaptic conductance, i.e., fixed self-synaptic conductance $g_{11} = g_{22} = 0$ (in the Figure 8) and $g_{11} = g_{22} = 0.2$ (in the Figure 9). When we fixed $g_{11} = 0.2$ and $g_{12} = 0.1$, we analyzed the synchronous branches of the HCO in the presence or absence of electromagnetic induction (in the Figure 7(a2),(a3)), respectively. It can be observed that the addition of electromagnetic induction fundamentally changes the phase difference of the HCO. We show the change in phase difference before and after the addition of electromagnetic induction in the Figure 7(b), which is obtained by taking the difference in phase difference at the corresponding points in the Figure 7(a2),(a3) as the dependent variable. The independent variables are conductance g_{21} and g_{22}. We will also discuss the discharge rhythm of the HCO under asymmetric self-coupling conductance (in the Figure 10).

We present the phase difference diagram of the HCO when electromagnetic induction stimulates neuron 1, and when the autapse conductance and mutual inhibition conductance are equal, respectively (in the Figure 7(a1)). We also calculated that when the autapse conductance and mutual inhibition conductance are equal (not shown in the Figure), the HCO, without introducing electromagnetic induction, is in an absolute and completely synchronized state. Here, Figure 8(b2) is a special case of complete synchronization (where $g_{11} = g_{22} = 0$, $g_{12} = g_{21} = 0.2$). At this point, whether reducing the conductance g_{12} to 0.02 or increasing g_{12} to 0.4 (in the Figure 8(b1),(b3)), not only will it change the synchronization state of the discharge patterns of the two neurons, but it will also affect the discharge rhythm patterns of the two neurons. We observed that the addition of electromagnetic induction to the synchronized state not only fundamentally altered the synchronization of the two neurons but also resulted in significant changes in the firing neuron rhythms (as shown in the Figure 8(a2)). This suggests that the discharge mode of the system in the synchronous state is more responsive to the addition of
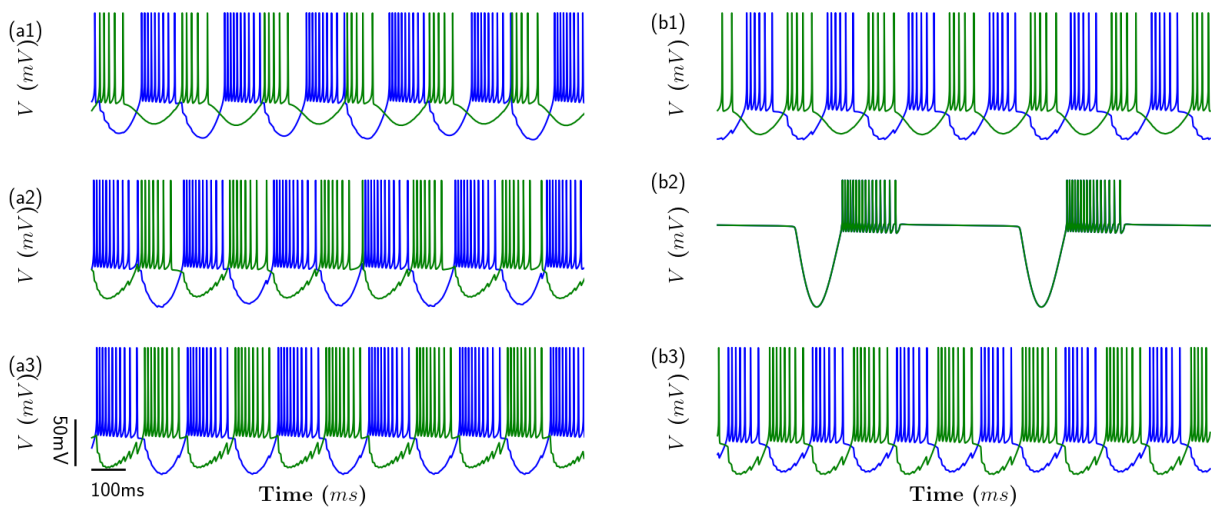
electromagnetic induction than the asynchronous rhythm modes. These findings are consistent with our previous analysis. The number of peaks in each neurons 1 and 2 burster in the HCO gradually increases as the conductance parameter g_{21} increases from 0.02 to 0.4. Electromagnetic induction seems to make the peak changes in the firing rhythm of neurons not continuous in each burst but rather a direct burst of multiple peaks. Therefore, electromagnetic induction has a more profound impact on the synchronization of HCOs.
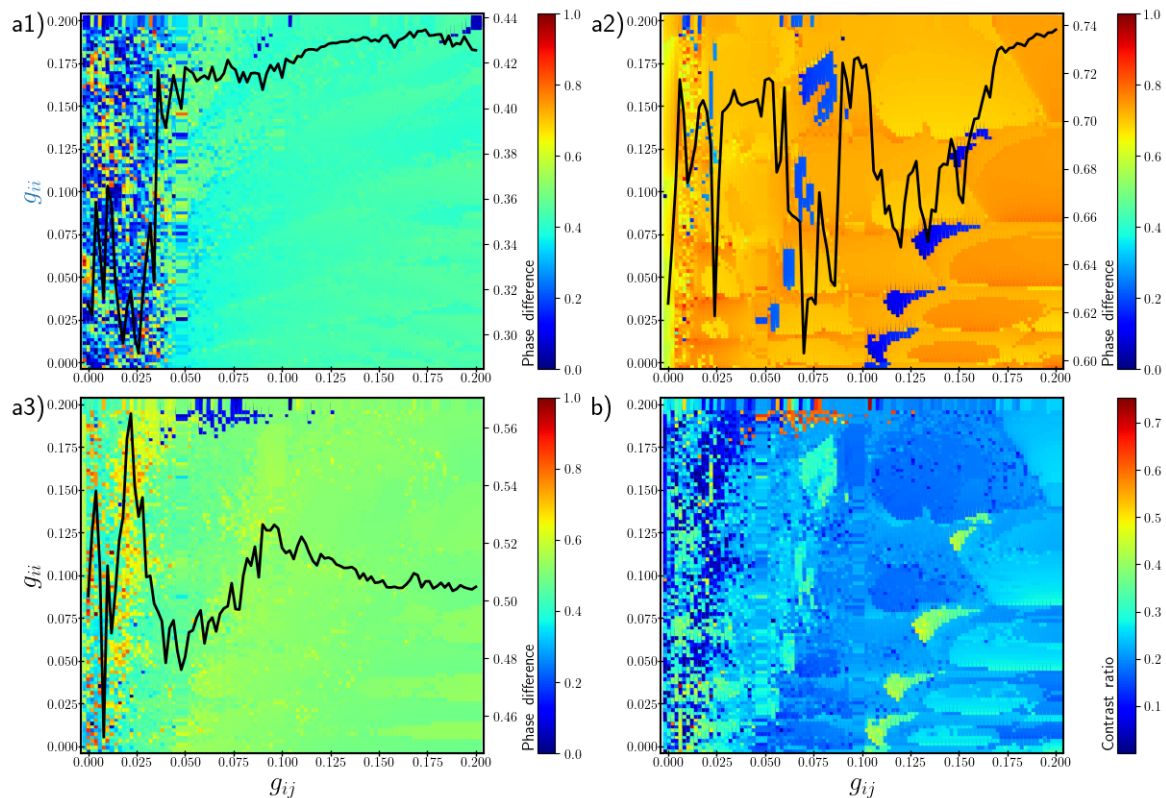
Figure 7. The combined effect of synaptic conductance g_{ii} and g_{ij} on synchronization in the HCO. The color bar indicates the phase difference $\Delta^{(n)}$, which is similar with the definition in Ref [45]. Dark blue zone corresponds to the zero phase difference (indicates complete synchronization). Dark red color indicates the maximum phase difference. Three black curves representing fixed horizontal axis values and the average phase difference (S) with changes in vertical axis values. (a1) When $g_{11} = g_{22} = g_{ii}$, $g_{12} = g_{21} = g_{ij}$, the phase difference diagram with changes in g_{ii} and g_{ij}, $k = 0.00005$, only stimulating neuron 1; (a2) Fix $g_{11} = 0.2, g_{12} = 0.1$, the phase difference diagram with changes in g_{21} and g_{22}, $k = 0$; (a3) Fix $g_{11} = 0.2, g_{12} = 0.1$, and the phase difference diagram with changes in g_{21} and g_{22}, $k = 0.00005$, only stimulating neuron 1; (b) Comparison chart of phase difference between (a2) and (a3).
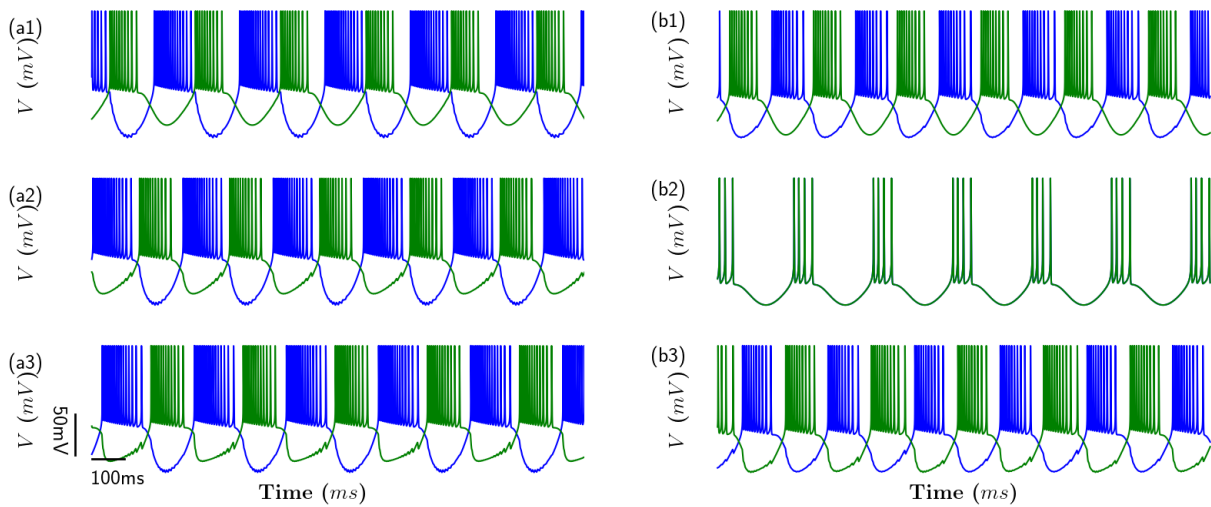
Figure 8. The discharge rhythm of the HCO when the autapse conductance $g_{11} = g_{22} = 0$. Here, g_{21} is fixed at 0.2. The conductance parameters g_{12} from top to bottom are 0.02, 0.2, and 0.4, respectively. On the right side, there is no electromagnetic induction; on the left, electromagnetic induction is added, and the parameter $k = 0.00005$ only stimulates neuron 1. Blue represents the membrane potential sequence of neuron 1, and green represents the membrane potential sequence of neuron 2.

Figure 9. The discharge rhythm of HCO varies with the parameter g_{12}, where $g_{21} = 0.2$ when $g_{11} = g_{22} = 0.2$. The conductance parameters g_{12} from top to bottom are 0.02, 0.2, and 0.4, respectively. On the right side, there is no electromagnetic induction, while on the left side, electromagnetic induction is added, and the parameter $k = 0.00005$ only stimulates neuron 1. Blue represents the membrane potential sequence of neuron 1, and green represents the membrane potential sequence of neuron 2.

According to the phase difference analysis above, the two neurons in the HCO exhibit a fully syn-

chronized state when the autapse conductance and mutual inhibition conductance are equal, respectively, and no electromagnetic induction is introduced (not shown in the Figure). Figure 8(b2) shows the discharge rhythm when $g_{11} = g_{22} = 0$. In the Figure 9(b2), neurons 1 and 2 demonstrate an HCO with synchronized discharge rhythm when autapse and mutual inhibition conductance parameters are 0.2. Here, we present the discharge rhythms of the HCO when the two autapse conductance parameters are equal to 0 and 0.2, respectively (in the Figure 8(b2) and Figure 9(b2)). It is evident that the conductance parameters of autapse significantly affect the neuron's discharge rhythm. With g_{12} reduced to 0.02 (in the Figure 9(b1)), synchronization disappears, peak count decreases, and amplitude increases. When increasing $g_{12} = 0.4$ (in the Figure 9(b3)), the synchronization state of the system will also disappear, the amplitude of the peaks will increase, and the number of peaks in each burster will decrease, but it is still more than when $g_{12} = 0.02$. In an HCO, the left side of Figure 9 is obtained when electromagnetic induction stimulates neuron 1, and we can see that the synchronization state of the system immediately disappears (in the Figure 9(a2)). Neuron 1 is more sensitive to electromagnetic induction when $g_{12} = 0.02$ (in the Figure 9(a1)), while at this time, neuron 2 has almost no change in the peak number of each burster except for the change in the initial discharge time of the burster. When the value of g_{12} is 0.4 (in the Figure 9(a3)), the changes in the firing rhythms of neurons 1 and 2 show an enhanced response to electromagnetic induction. From the variation of the discharge rhythm from top to bottom on the left side, we can see that the larger the g_{12}, the better the robustness of the HCO, and the discharge rhythm in the synchronous state is more sensitive to the intervention of electromagnetic induction.
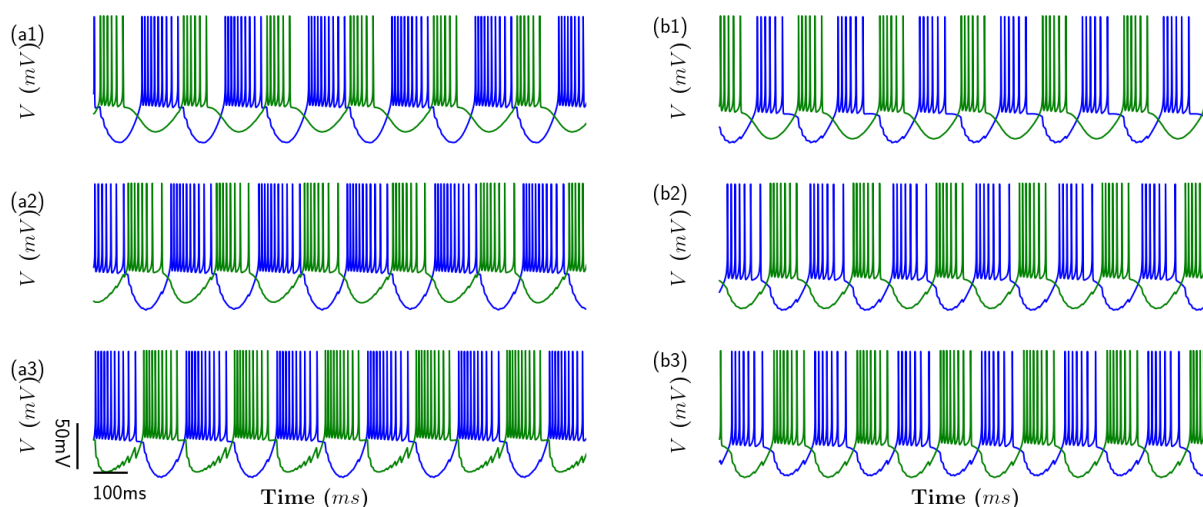
Figure 10. The discharge rhythm of HCOs varies with g_{12} when $g_{11} = 0.2$ and $g_{22} = 0.1$, where $g_{21} = 0.2$. The conductance parameters g_{12} from top to bottom are 0.02, 0.1, and 0.4, respectively. There is no electromagnetic induction on the right side, but there is electromagnetic induction on the left side that only stimulates neuron 1 with the parameter $k = 0.00005$. Blue represents the membrane potential sequence of neuron 1, and green represents the membrane potential sequence of neuron 2.

Previously, we discussed the discharge rhythms of HCOs in two cases where the conductance of two autapses is equal. Here, we will consider the discharge rhythm of the HCO at $g_{11} = 0.2$, $g_{12} = 0.1$, $g_{21} =$

0.2, and $g_{22} = 0.1$ (in the Figure 10(a2),(b2)), that is, how the discharge rhythm of the HCO changes when the autapse conductance is not equal (corresponding to a position point in the Figure 7(a2),(a3)). In addition, we also discussed the discharge rhythms of the system at $g_{12} = 0.02$ and 0.4, as shown in the Figure 10 (a1),(b1),(a3),(b3), respectively. Compared with Figure 9(b2) ($g_{12} = g_{22} = 0.2$), here we change g_{12} and g_{22} from 0.2 to 0.1, respectively, to obtain Figure 10(b2) ($g_{12} = g_{22} = 0.1$). The number of bursts and the intensity of the burst mode vary considerably. The discharge timing of the burster mode has undergone significant changes. When the value of g_{12} is 0.02, the firing rhythm of neuron 1 is significantly affected by electromagnetic induction. The peak number of each burster in neuron 2 remains unchanged, but the firing time of the burster mode is changing (in the Figure 10(a1)). When g_{12} increases by 0.1 or 0.4, the HCO becomes more sensitive to the addition of electromagnetic induction (in the Figure 10(a2),(a3)). The firing rhythm of neuron 1 directly receiving electromagnetic induction stimulation will undergo fundamental changes. The left panel of Figure 10 shows the firing rhythm of neuron 2. The larger the conductance g_{12}, the better the robustness of the system, which is consistent with our previous analysis (in the Figure 9). Here, we discuss the changes in the HCO discharge patterns of symmetric autapse (in the Figures 8 and 9) and asymmetric autapse (in the Figure 10), as well as the influence of electromagnetic induction on the discharge patterns. It is important to consider the connection modes of autapse and non-autapse connections.

4. Conclusions

In this article, we analyze the discharge rhythm of an individual neuron model under electromagnetic induction and demonstrate it as a classical burster pattern. We show the time series of slow variables, gate variables, and the electromagnetic induction term $\rho(\phi)$. It is found that the electromagnetic induction term $\rho(\phi)$ has a minor regulatory effect on the firing rhythm of neurons compared to slow variables. Moreover, we demonstrate an individual neuron's fast-slow dynamics branch diagram, which varies with different electromagnetic induction parameters. We discover that electromagnetic induction has a profound impact on the dynamic characteristics of individual neurons. Next, we examined the firing rhythms of three groups of neurons with different slow variable parameters ε. We concluded that the addition of electromagnetic induction fundamentally changes the firing rhythm of an individual neuron. We are interested in the effect of electromagnetic induction on the HCO. Here, we examine the improved HCO discharge mode, which includes the addition of autapse. The impact of autapse and mutually inhibitory synapses under electromagnetic induction on the rhythmic patterns of the HCO are considered (in the Figures 5 and 6). When the synaptic parameter values are the same, there is a significant difference in the performance of self-inhibitory synaptic and mutually inhibitory synaptic discharge patterns. Electromagnetic induction affects the discharge rhythm of the HCO differently based on the type of synapses, whether self-inhibitory or mutually inhibitory. Therefore, it is essential to take note of the connection modes of the synapses during the experiment.

Furthermore, we investigate the synchronization phenomenon of the improved HCO. The change in phase difference of the HCO with and without the introduction of electromagnetic induction is analyzed when synaptic parameters change. We discuss a comparison plot of the phase difference before and after the introduction of electromagnetic induction, which more intuitively shows the change in phase difference caused by the introduction of electromagnetic induction. By further exploring the discharge modes of the HCO and summarizing the changes in the discharge modes of the two sym-

metric autapses (in the Figures 8 and 9), it can be found that the discharge mode in the synchronous state of the system has a more robust response to electromagnetic induction compared to the asynchronous rhythmic mode. It is apparent that the larger the conductance g_{12}, the greater the robustness of the HCO. At the same time, the discharge rhythm of neuron 1 directly receiving electromagnetic induction stimulation changes significantly, while the discharge rhythm of neuron 2 passively receiving stimulation is affected by the value of g_{12}. The larger the value of g_{12}, the stronger the response of neuron 2. Finally, we analyze the changes in the discharge mode of the HCO with changes in synaptic conductance parameters under asymmetric autapse. The response patterns of the HCO of symmetric and asymmetric autapse to electromagnetic induction are different, manifested by the diverse discharge modes of the HCO.

Therefore, these rules of the HCO need to be paid attention to, including different synaptic connections, the response of different synaptic connections to electromagnetic induction, the different effects of electromagnetic induction on its synchronization, and the different effects of symmetric and asymmetric autapse on the discharge mode of the HCO. In our study, we examined chemical synapses between neurons and did not consider any electrical coupling that may have been present between them. In future studies, we will analyze the synergistic effects of electrical and chemical coupling in HCO or CPG, which can lead to very different rhythmic patterns. Our current model demonstrates that synaptic conductance can influence the rhythm pattern of the HCO. The diversity of rhythm activities in CPG is essential for its flexibility and robustness, which can resist interference from external information. Synaptic conductance and electromagnetic induction changes can produce many different rhythm activities, making the CPG less susceptible to external interference. Of course, the relationship between rhythmic activities of HCO (or CPG) and epilepsy and other diseases will also be paid attention to.

Use of AI tools declaration

The authors declare they have not used Artificial Intelligence (AI) tools in the creation of this article.

Acknowledgments

Conflict of interest

The authors declare there is no conflicts of interest.

References

1. E. Marder, D. Bucher, Central pattern generators and the control of rhythmic movements, *Curr. Biol.*, **11** (2001), R986–R996. https://doi.org/10.1016/S0960-9822(01)00581-4

2. E. Marder, R. L. Calabrese, Principles of rhythmic motor pattern generation, *Physiol. Rev.*, **76** (1996), 687–717. https://doi.org/10.1152/physrev.1996.76.3.687

3. D. N. Masaev, A. A. Suleimanova, N. V. Prudnikov, M. V. Serenko, A. V. Emelyanov, V. A. Demin, et al., Memristive circuit-based model of central pattern generator to reproduce spinal neuronal activity in walking pattern, *Front. Neurosci.*, **17** (2023), 1124950. https://doi.org/10.3389/fnins.2023.1124950

4. D. Alaçam, A. Shilnikov, Making a swim central pattern generator out of latent parabolic bursters, *Int. J. Bifurcation Chaos*, **25** (2015), 1540003. https://doi.org/10.1142/S0218127415400039

5. E. Marder, S. Kedia, E. O. Morozova, New insights from small rhythmic circuits, *Curr. Opin. Neurobiol.*, **76** (2022), 102610. https://doi.org/10.1016/j.conb.2022.102610

6. E. Marder, Neuromodulation of neuronal circuits: back to the future, *Neuron*, **76** (2012), 1–11. https://doi.org/10.1016/j.neuron.2012.09.010

7. T. Nowotny, M. I. Rabinovich, Dynamical origin of independent spiking and bursting activity in neural microcircuits, *Phys. Rev. Lett.*, **98** (2007), 128106. https://doi.org/10.1103/PhysRevLett.98.128106

8. M. Lodi, A. L. Shilnikov, M. Storace, Design principles for central pattern generators with preset rhythms, *IEEE Trans. Neural Networks Learn. Syst.*, **31** (2019), 3658–3669. https://doi.org/10.1109/TNNLS.2019.2945637

9. J. T. C. Schwabedal, A. B. Neiman, A. L. Shilnikov, Robust design of polyrhythmic neural circuits, *Phys. Rev. E*, **90** (2014), 022715. https://doi.org/10.1103/PhysRevE.90.022715

10. J. Collens, K. Pusuluri, A. Kelley, D. Knapper, T. Xing, S. Basodi, et al., Dynamics and bifurcations in multistable 3-cell neural networks, *Chaos*, **30** (2020), 072101. https://doi.org/10.1063/5.0011374

11. Q. Lu, J. Tian, Synchronization and stochastic resonance of the small-world neural network based on the CPG, *Cognit. Neurodyn.*, **8** (2014), 217–226. https://doi.org/10.1007/s11571-013-9275-8

12. Y. Zang, S. Hong, S. E. De, Firing rate-dependent phase responses of Purkinje cells support transient oscillations, *eLife*, **9** (2020), e60692. https://doi.org/10.7554/eLife.60692

13. B. S. Gutkin, G. B. Ermentrout, A. D. Reyes, Phase-response curves give the responses of neurons to transient inputs, *J. Neurophysiol.*, **94** (2005), 1623–1635. https://doi.org/10.1152/jn.00359.2004

14. Y. Zang, E. Marder, Neuronal morphology enhances robustness to perturbations of channel densities, *PNAS*, **120** (2023), e2219049120. https://doi.org/10.1073/pnas.2219049120

15. E. M. Izhikevich, Neural excitability, spiking, and bursting, *Int. J. Bifurcation Chaos*, **10** (2000), 1171–1266. https://doi.org/10.1142/S0218127400000840

16. B. Lu, X. Jiang, Reduced and bifurcation analysis of intrinsically bursting neuron model, *Electron. Res. Arch.*, **31** (2023), 5928–5945. https://doi.org/10.3934/era.2023301

17. F. Zhan, S. Liu, X. Zhang, J. Wang, B. Lu, Mixed-mode oscillations and bifurcation analysis in a pituitary model, *Nonlinear Dyn.*, **94** (2018), 807–826. https://doi.org/10.1007/s11071-018-4395-7

18. H. Zhou, B. Lu, H. Gu, X. Wang, Y. Liu, Complex nonlinear dynamics of bursting of thalamic neurons related to Parkinson's disease, *Electron. Res. Arch.*, **32** (2024), 109–133. https://doi.org/10.3934/era.2024006

19. Z. Song, J. Xu, Codimension-two bursting analysis in the delayed neural system with external stimulations, *Nonlinear Dyn.*, **67** (2012), 309–328. https://doi.org/10.1007/s11071-011-9979-4

20. W. B. Kristan, Neuronal decision-making circuits, *Curr. Biol.*, **18** (2008), R928–R932. https://doi.org/10.1016/j.cub.2008.07.081

21. K. L. Briggman, W. B. Kristan, Multifunctional pattern-generating circuits, *Annu. Rev. Neurosci.*, **31** (2008), 271–294. https://doi.org/10.1146/annurev.neuro.31.060407.125552

22. J. Wojcik, J. Schwabedal, R. Clewley, A. L. Shilnikov, Key bifurcations of bursting polyrhythms in 3-cell central pattern generators, *PLoS One*, **9** (2014), e92918. https://doi.org/10.1371/journal.pone.0092918

23. C. A. Tassinari, G. Cantalupo, B. Hoegl, P. Cortelli, L. Tassi, S. Francione, et al., Neuroethological approach to frontolimbic epileptic seizures and parasomnias: the same central pattern generators for the same behaviours, *Rev. Neurol.*, **165** (2009), 762–768. https://doi.org/10.1016/j.neurol.2009.08.002

24. C. A. Tassinari, E. Gardella, G. Cantalupo, G. Rubboli, Relationship of central pattern generators with parasomnias and sleep-related epileptic seizures, *Sleep Med. Clin.*, **7** (2012), 125–134. https://doi.org/10.1016/j.jsmc.2012.01.003

25. F. Zhan, J. Song, S. Liu, The influence of synaptic strength and noise on the robustness of central pattern generator, *Electron. Res. Arch.*, **32** (2024), 686–706. https://doi.org/10.3934/era.2024033

26. V. Baruzzi, M. Lodi, M. Storace, A. Shilnikov, Towards more biologically plausible central-pattern-generator models, *Phys. Rev. E*, **104** (2021), 064405. https://doi.org/10.1103/PhysRevE.104.064405

27. R. L. Calabrese, Half-center oscillators underlying rhythmic movements, in *The Handbook of Brain Theory and Neural Networks*, (1998), 444–447.

28. A. Sakurai, P. S. Katz, The central pattern generator underlying swimming in Dendronotus iris: a simple half-center network oscillator with a twist, *J. Neurophysiol.*, **116** (2016), 1728–1742. https://doi.org/10.1152/jn.00150.2016

29. A. Doloc-Mihu, R. L. Calabrese, A database of computational models of a half-center oscillator for analyzing how neuronal parameters influence network activity, *J. Biol. Phys.*, **37** (2011), 263–283. https://doi.org/10.1007/s10867-011-9215-y

30. A. Doloc-Mihu, R. L. Calabrese, Analysis of family structures reveals robustness or sensitivity of bursting activity to parameter variations in a half-center oscillator (HCO) model, *eNeuro*, **3** (2016). https://doi.org/10.1523/ENEURO.0015-16.2016

31. Z. Song, J. Xu, Multiple switching and bifurcations of in-phase and anti-phase periodic orbits to chaotic coexistence in a delayed half-center CPG oscillator, *Nonlinear Dyn.*, **111** (2023), 16569–16584. https://doi.org/10.1007/s11071-023-08670-w

32. Z. Song, J. Xu, Multi-coexistence of routes to chaos in a delayed half-center oscillator (DHCO) system, *Nonlinear Dyn.*, **112** (2024), 1469–1486. https://doi.org/10.1007/s11071-023-09089-z

33. A. J. White, Sensory feedback expands dynamic complexity and aids in robustness against noise, *Biol. Cybern.*, **116** (2022), 267–269. https://doi.org/10.1007/s00422-021-00917-2

34. F. Zhan, S. Liu, Response of electrical activity in an improved neuron model under electromagnetic radiation and noise, *Front. Comput. Neurosci.*, **11** (2017), 107. https://doi.org/10.3389/fncom.2017.00107

35. Z. Wang, Y. Yang, L. Duan, Control effects of electromagnetic induction on epileptic seizures, *Nonlinear Dyn.*, **112** (2024). https://doi.org/10.1007/s11071-024-09373-6

36. A. S. Lele, Y. Fang, J. Ting, A. Raychowdhury, Learning to walk: bio-mimetic hexapod locomotion via reinforcement-based spiking central pattern generation, *IEEE J. Emerging Sel. Top. Circuits Syst.*, **10** (2020), 536–545. https://doi.org/10.1109/JETCAS.2020.3033135

37. T. Sun, Z. Dai, P. Manoonpong, Distributed-force-feedback-based reflex with online learning for adaptive quadruped motor control, *Neural Networks*, **142** (2021), 410–427. https://doi.org/10.1016/j.neunet.2021.06.001

38. B. Muthuswamy, Implementing memristor based chaotic circuits, *Int. J. Bifurcation Chaos*, **20** (2010), 1335–1350. https://doi.org/10.1142/S0218127410026514

39. M. Lv, C. Wang, G. Ren, J. Ma, X. Song, Model of electrical activity in a neuron under magnetic flow effect, *Nonlinear Dyn.*, **85** (2016), 1479–1490. https://doi.org/10.1007/s11071-016-2773-6

40. F. Zhan, S. Liu, J. Wang, B. Lu, Bursting patterns and mixed-mode oscillations in reduced Purkinje model, *Int. J. Mod. Phys. B*, **32** (2018), 1850043. https://doi.org/10.1142/S0217979218500431

41. D. Terman, J. E. Rubin, A. C. Yew, C. J. Wilson, Activity patterns in a model for the subthalamopallidal network of the basal ganglia, *J. Neurosci.*, **22** (2002), 2963–2976. https://doi.org/10.1523/JNEUROSCI.22-07-02963.2002

42. F. Su, J. Wang, S. Niu, H. Li, B. Deng, C. Liu, et al., Nonlinear predictive control for adaptive adjustments of deep brain stimulation parameters in basal ganglia–thalamic network, *Neural Networks*, **98** (2018), 283–295. https://doi.org/10.1016/j.neunet.2017.12.001

43. J. Song, S. Liu, H. Lin, Model-based quantitative optimization of deep brain stimulation and prediction of Parkinson's states, *Neuroscience*, **498** (2022), 105–124. https://doi.org/10.1016/j.neuroscience.2022.05.019

44. J. Song, H. Lin, S. Liu, Basal ganglia network dynamics and function: role of direct, indirect and hyper-direct pathways in action selection, *Network: Comput. Neural Syst.*, **34** (2023), 84–121. https://doi.org/10.1080/0954898X.2023.2173816

45. Z. Song, F. Ji, J. Xu, Is there a user-friendly building unit to replicate rhythmic patterns of CPG systems? Synchrony transition and application of the delayed bursting-HCO model, *Chaos, Solitons Fractals*, **182** (2024), 114820. https://doi.org/10.1016/j.chaos.2024.114820